Direct numerical simulation of flame-wall interaction at gas turbine relevant conditions

Direct Numerical Simulation of Flame-Wall Interaction at Gas Turbine Relevant Conditions

Kai Niemietz[a,*], Lukas Berger[a], Michael Huth[b], Antonio Attili[c], Heinz Pitsch[a]

[a] *Institute for Combustion Technology, RWTH Aachen University, 52056 Aachen, Germany*
[b] *Siemens Energy Global GmbH & Co. KG, Mellinghofer Str. 55, 45473 Mülheim an der Ruhr, Germany*
[c] *Institute for Multiscale Thermofluids, School of Engineering, University of Edinburgh, Edinburgh, EH9 3FD, United Kingdom*

Abstract

A direct numerical simulation (DNS) with finite rate chemistry was performed to evaluate the main influences on carbon monoxide (CO) emissions in gas turbine combustion. A lean methane/air mixture is burned in fully turbulent jet flames in a domain enclosed by isothermal walls. The formation of CO is found to be affected by the mean strain rate of the turbulent flow, the flame-wall interaction (FWI), and the interactions of the flame with the recirculation zones of the flow. The CO production and consumption in the turbulent flame differ strongly from the reaction rates in a freely propagating flame. In the upstream part of the domain, the mean strain rate of the turbulent flow mainly affects the CO formation, while wall heat loss influences the CO oxidation process towards the end of the domain, where the strain rate decreases. In an optimal estimator analysis, the relevant parameters that dominate the formation and consumption of CO are identified as the local CO mass fraction Y_{CO}, the wall heat loss, described by the enthalpy defect Δh, and the mass fraction of the OH radical Y_{OH}. The heat loss is particularly influential close to the wall while the effects far from the wall are negligible. Using the local CO mass fraction as parameter describes the late-stage oxidation of CO well in the entire domain. In particular, Y_{CO} should not be neglected at the wall. Y_{OH} is well suited to describe the processes involved in CO oxidation, as it both parameterizes the turbulent strain and is the main reaction partner for CO oxidation. The combination of Y_{CO} and Δh was able to improve the domain-averaged irreducible error by almost half compared to only a progress variable. Adding Y_{OH} to the parameter set further reduced the error to 25% of the original error.

Keywords: Direct Numerical Simulation; Flame-Wall Interaction; CO Emissions; Gas Turbine Combustion

1. Introduction

Gas turbines can play an important role as a bridge technology towards reduced carbon emissions and a cleaner energy sector. Their carbon dioxide (CO_2) emissions are significantly lower than most conventional power plants and their start-up times are comparably low. This makes gas turbines predestined to load-balance an electrical grid with decentralized, fluctuating, renewable energy contributions. However, the load flexibility of gas turbines is limited by an increase of carbon monoxide (CO) emissions at low load conditions [1, 2]. Optimizing gas turbine designs to enable lower load limits requires a comprehensive assessment of various influences on the formation of CO emissions. In this paper, we investigate the effects of flame-wall interactions (FWI) and the mean strain rate in a turbulent flow on CO, its oxidation, and possible emissions.

The impact of FWI on flame dynamics and combustion chemistry has been studied in various configurations [3]. Here, we want to focus on CO emissions resulting from FWI. The effect of FWI on CO chemistry in premixed methane/air flames has been studied both experimentally and numerically [4–9]. Mann et al. [4] investigated 1D head on quenching (HOQ) flames experimentally and found increased CO concentrations close to the cold wall. They further found that the CO increase is more pronounced for leaner flames. Jainski et al. [5] reported a shift of peak CO concentration towards the wall as the flame approaches the wall in an experimental laminar side wall quenching (SWQ) setup. These findings were confirmed by a numerical investigation by Ganter et al. [6] who attributed the increased CO concentration at the wall to transport, originating far away from the wall. Palulli et al. [9] investigated a 2D laminar flame with velocity fluctuations and showed that CO concentrations are influenced by the flame surface orientation close to the wall. They reported that both convective and diffusive transport is present and that the respective contributions vary with the velocity fluctuations. Very recently, Jiang et al. [10] and Palulli et al. [11] investigated FWI in turbulent channels with V-shaped flames. Jiang et al. found that an ensemble of 1D flamelets with various initial temperatures and strain rates was able to capture CO behavior, except close to the wall and suggest that a species transport budget might be needed. Further research is necessary to understand the transport budget in the full range of velocity scales present in turbulent combustion.

Two of the prevalent approaches in the literature to model CO emissions are flamelet progress variable (FPV) models or flamelet generated manifolds (FGM). One focus of the current research is the improvement of these models by increasing the dimensionality of the tabulation and the complexity of the 1D flames used to create the tables/manifolds [12, 13]. Kosaka et al. [12] demonstrated that 1D flamelets with an enthalpy defect term improve CO predictions over an adiabatic model, except in the wall quenching region. Efimov et al. [13] modeled FWI with a 3D flamelet generated manifold (FGM) of 1D HOQ flames using a progress variable, enthalpy, and the wall heat loss rate as parameters.

The prediction of CO is challenging not only in the scope of FWI. Because the chemical timescales of CO are long, transport processes influence the oxidation of CO in unconstrained flows as well [14]. A promising approach is the solution of an additional transport equation for CO. Such an approach for slow chemical species for has been proposed and investigated by Ihme & Pitsch [15] for nitric oxide (NO). Trisjono et al. [16] implemented a transport equation for NO with an enthalpy defect to account for heat loss. In recent years, this idea has been extended to CO chemistry by Han et al. [17] and Popp et al. [14]. Han et al. compared results from finite rate chemistry to strained and unstrained flamelets and found that a table of several differently strained flamelets was necessary to accurately capture the flame structure.

In this investigation, we study CO emissions in the context of turbulent premixed jet flames that are bounded by isothermal walls. We have a high wall temperature, elevated inlet temperature and pressure, and low equivalence ratio, representing gas turbine conditions. As the effects of strain rate and FWI are shown to be important, the present DNS case features strong contributions of both phenomena to investigate the individual contributions and possible joint interactions. The aim is to understand and quantify the contributions of the different physical phenomena.

The simulation setup and numerical methods are presented in section 2, results and discussion are found in section 3, and section 4 offers a summary and conclusions.

2. Configuration and numerical methods

The simulation domain is set up to capture most relevant effects in gas turbine combustion including high strain rates due to the turbulent flow, large areas of strong FWI, and two distinct recirculation regions, where cooled, burnt gas interacts with the flame. As shown in Fig 1, the inlet consists of two parallel turbulent slot jets, separated by a laminar pilot. Isothermal, no-slip walls enclose the domain in the crosswise direction; periodic boundary conditions are implemented in the spanwise direction.

The bulk inlet velocity of the jets is $u_\mathrm{j} = 73.5\,\mathrm{m/s}$ and the jet width is $h_\mathrm{j} = 1.2\,\mathrm{mm}$ resulting in a jet Reynolds number ($\mathrm{Re_j} = u_\mathrm{j} h_\mathrm{j}/\nu$) of 5500, with the kinematic viscosity of the reactants ν. The unburnt mixture consists of premixed methane/air with an equivalence ratio of $\varphi = 0.5$ and an unburnt temperature of $673\,\mathrm{K}$. The jets' inlet velocity fields are obtained from two statistically independent auxiliary simulations of fully developed turbulent channel flows. The laminar pilot has an inlet velocity of $u_\mathrm{p} = 20\,\mathrm{m/s}$ and consists of burnt gas corresponding to the jet inlet conditions. The pilot inlet parameters were chosen to create a jet to pilot fuel ratio of $9/1$

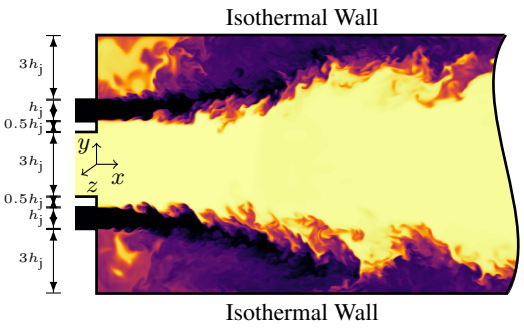

Fig. 1: Sketch of the simulation domain. Color indicates the temperature field. The inflow consists of two turbulent jets with a pilot in the center.

matching typical gas turbine values. The pressure is set to $4\,\mathrm{bar}$ and the wall temperatures of the crosswise boundaries are fixed at $T_\mathrm{w} = 1000\,\mathrm{K}$. The wall temperature is set relatively high, between the unburnt and burnt temperatures of the fluid to mimic typical conditions in gas turbine combustors. The domain extends to $100h_\mathrm{j}$ in streamwise direction, x, $12h_\mathrm{j}$ and $6h_\mathrm{j}$ in cross- and spanwise directions, y and z. The streamwise and spanwise spatial resolutions Δ are $20\,\mu\mathrm{m}$; in crosswise direction, Δ is reduced to $10\,\mu\mathrm{m}$ to adequately resolve the flow towards the wall, yielding a y^+ value below unity at all locations. The thermal flame thickness of the unstretched laminar flame is $l_\mathrm{F} = 205\,\mu\mathrm{m}$ and thus resolved with 10 gridpoints. The resolution is chosen such that the Kolmogorov length scale η is well resolved ($\Delta/\eta < 2$) at all times and all spatial positions [18]. η is computed as $\eta = (\overline{\nu}^3/\widetilde{\varepsilon})^{1/4}$, where $\widetilde{\varepsilon}$ is the density-weighted ensemble-averaged dissipation rate and $\overline{\nu}$ is the ensemble-averaged viscosity [18]. Additional grid convergence results are available in the supplementary material. The resulting simulation grid contains 3.1 billion cells. The reactive, unsteady Navier-Stokes equations are solved in the low-Mach limit using the in-house finite-differences solver CIAO [19]. All transport coefficients are determined with unity Lewis number. This assumption was made to remove interactions of differential diffusion effects and turbulence, and instead provide a dataset in which the effects of wall heat losses on the CO formation can be isolated and rigorously studied. This allows us to understand and develop models for CO emissions without the additional complexity of differential diffusion. Furthermore, the chemical states produced by assuming unity Lewis numbers might be closer to those encountered in realistic high Reynolds number combustion processes where mixing is more governed by turbulence than by molecular transport. The simulations include finite rate chemistry. A reduced mechanism for lean methane combustion with 25 species and 155 reactions was derived from the full mechanism developed by Cai et al. [20]. All relevant parameters of the simulation setup are collected in table 1.

Table 1: Simulation parameters, initial and boundary conditions. The Kolmogorov lengthscale and the Karlovitz number are evaluated on the flame surface, defined by maximum heat release ($C = 0.1236$).

$L_x \times L_y \times L_z\,(h_\mathrm{j})$	$100 \times 12 \times 6$
$\Delta_x \times \Delta_y \times \Delta_z\,(\mu\mathrm{m})$	$20 \times 10 \times 20$
φ	0.5
$p\,(\mathrm{bar})$	4
$T^u\,(\mathrm{K})$	673
$T^b\,(\mathrm{K})$	1782
$T_\mathrm{w}\,(\mathrm{K})$	1000
$u_\mathrm{j}\,(\mathrm{m/s})$	73.5
$h_\mathrm{j}\,(\mathrm{mm})$	1.2
$\mathrm{Re_j}$	5500
$s_\mathrm{L}\,(\mathrm{cm/s})$	27.37
$l_\mathrm{F}\,(\mu\mathrm{m})$	205
$\tau_\mathrm{F}\,(\mu\mathrm{s})$	749
$\eta\,(\mu\mathrm{m})$	11
Ka	$45 - 192$

3. Results and discussion

3.1. Overview of the simulation

The simulation results are introduced in Fig. 2, where the temporally and spatially averaged velocity, temperature, CO mass fraction, and CO source term are shown. The streamwise velocity shows the average flow field in the domain. Because there is no co-flow above and below the turbulent jets, vortical structures develop in the top and bottom left corners of the domain and cause the jets to spread out towards the walls. With the main momentum flowing along the walls, a second recirculation area develops in the center of the domain before the two jets converge after $60h_\mathrm{j}$ and the flow field transitions into a channel-type flow. The flame shape is strongly influenced by the velocity field, as is visible from the temperature field. After $10h_\mathrm{j}$, the two jet flames are entirely attached to the combustor walls, featuring strong FWI and flame quenching at the wall. This slows the consumption of methane and lengthens the flames; the flame length is $55h_\mathrm{j}$. CO is mainly formed in a narrow band along the inside of the flame length and rapidly oxidized creating a sharp peak of high CO concentration. The width of this peak increases along the flame length and forms a large area of high CO at the flame tip. This widening is linked to the decrease of strain along the flame length and will be discussed in the following sections.

3.2. Mass fraction fluxes

Average streamwise fluxes of methane and CO mass fractions are presented in Fig. 3 along with the Favre-averaged temperature $\widetilde{T}$ along the streamwise axis. The average mass fraction fluxes are calculated as the crosswise and spanwise integral, with the den-

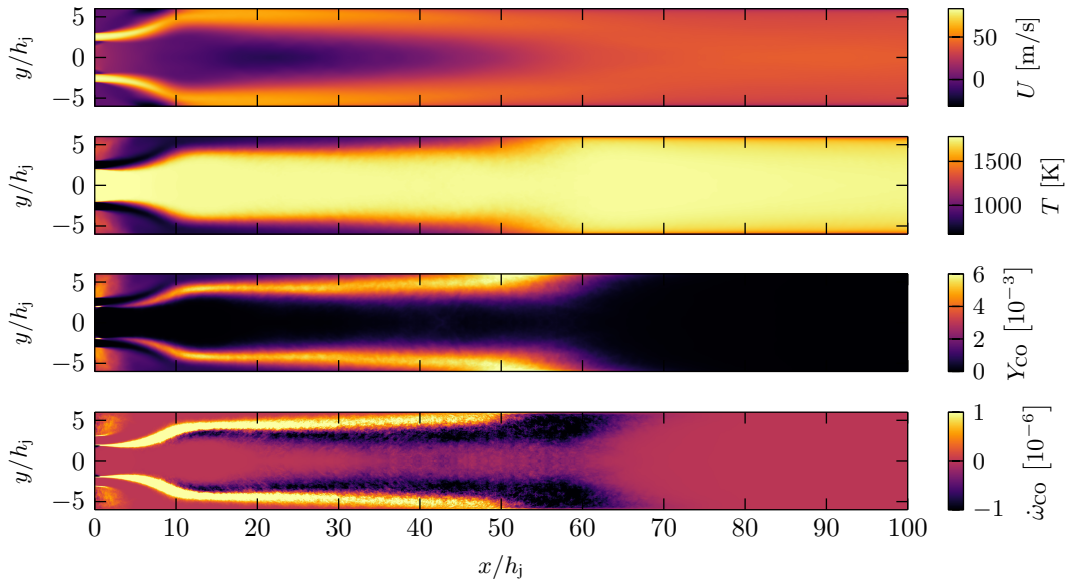

Fig. 2: Temporally and spatially averaged fields of the streamwise velocity component U, temperature T, CO mass fraction Y_CO, and CO source term $\dot{\omega}_\mathrm{CO}$.

sity ρ and the streamwise velocity component U:

$$\mathcal{Y}_\alpha = \frac{\int\int \rho \cdot U \cdot Y_\alpha \, dy \, dz}{\int\int \rho \cdot U \, dy \, dz}, \quad \alpha = \mathrm{CO}, \mathrm{CH_4} \quad (1)$$

Methane is slowly but consistently consumed along the flame length and is completely depleted at $x \approx 65 h_\mathrm{j}$, well before the end of the domain. After an initial steep increase, the CO concentration reaches a plateau region not typically seen in unconstrained jet flames. After the methane is completely consumed, most CO is oxidized quickly in this area of high temperature. However, a significant portion remains and oxidation slows as the temperature is reduced downstream. The CO concentration remains significantly higher than the equilibrium value that corresponds to the local temperature, throughout the domain. Using the outlet temperature to predict CO emissions leads to an underprediction of more than 50%.

To describe the combustion process, we chose a linear combination of species mass fraction as the progress variable as

$$C = Y_{\mathrm{H_2}} + Y_{\mathrm{H_2O}} + Y_\mathrm{CO} + Y_{\mathrm{CO_2}} \, . \quad (2)$$

In Fig. 4, the average CO mass fraction in the DNS is compared to the simple flamelet progress variable (FPV) model, where the CO mass fraction is retrieved from an unstretched premixed flamelet based on the previously defined progress variable. The local progress variable is calculated from the DNS data according to Eq. 2, the corresponding CO mass fraction is retrieved from the unstretched flamelet and mapped to the DNS field in an a-priori manner. Then, the local CO values (from FPV) are temporally and spatially averaged. This is a very simplistic approach, but

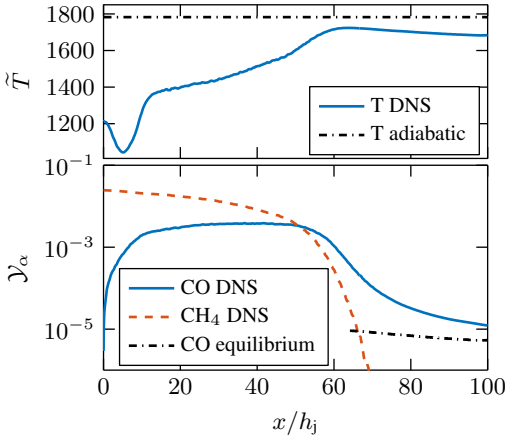

Fig. 3: Average streamwise flux of the methane and CO mass fractions and average temperature. Included are the CO equilibrium and the adiabatic flame temperature.

it serves to highlight possible errors. More accurate representations are investigated later. Two regions of different behavior are apparent: first, the FPV model overestimates the initial CO production and second, the FPV model does not account for the slow, continuous oxidation of CO in the post flame region. Instead of the gradual oxidation seen in the DNS data, the CO concentration remains almost constant in the last part of the domain. This discrepancy in the post-flame region, in particular, highlights the need for more accurate models that account for the physical phenomena occurring in complex flames.

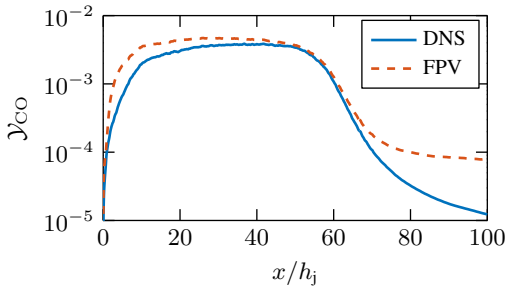

Fig. 4: Average CO flux in the domain compared to the CO flux calculated from the FPV model.

3.3. Effects of strain

First, we focus on the CO overestimation in the first third of the domain, where the average CO flux is lower than that obtained from the FPV model. The turbulent flow in this region leads to strain effects influencing the flame [21]. Fig. 5(a) shows the joint probability density function (jPDF) of Y_{CO} and T at a streamwise location of $10h_j$. Included are an unstrained flamelet and strained flamelets with strain rates between $a = 5000\,s^{-1}$ and $30\,000\,s^{-1}$. The tangential strain in a turbulent flame may be calculated from the velocity and progress variable fields as $a = \nabla \cdot \mathbf{u} - \mathbf{n} \cdot \nabla \mathbf{u} \cdot \mathbf{n}$, where $\mathbf{u}$ is the velocity vector and $\mathbf{n} = -\nabla C/|\nabla C|$ is the normal vector to the progress variable surface pointing towards the reactants [22]. The tangential strain in the DNS at $10h_j$ is in a range between $a = 5000\,s^{-1}$ and $40\,000\,s^{-1}$. The range of strain rates of the 1D flamelets corresponds well to the strain rates found in the DNS. An ensemble of several strained flamelets is best able to capture the distribution of Y_{CO} and T. In this first section of the domain, strain is the main influence on combustion. This is in part because the flame does not interact directly with the wall, but is separated from the wall by a layer of unburnt gas. While enthalpy loss leads to lower CO concentrations, the enthalpy loss necessary to account for the low CO concentrations is significantly higher than the enthalpy loss seen in the data. A figure comparing the DNS data to flamelets with reduced enthalpy is included in the supplementary material to illustrate this point. Knudsen et al. [23] investigated H and OH radicals as parameterizations for strain in turbulent combustion and found both to be well suited due to their uniqueness and high sensitivity to strain. They recommended H due to its low Lewis number and its consequent ability to account for differential diffusion effects. In this investigation we chose OH, because it is more relevant to CO oxidation and transport is consider with unity Lewis number.

Further downstream, the flame comes into closer contact with the wall and heat losses become relevant. Fig. 5(b) again shows the jPDF of Y_{CO} and T, but close to the flame tip ($50h_j$). Here, also the

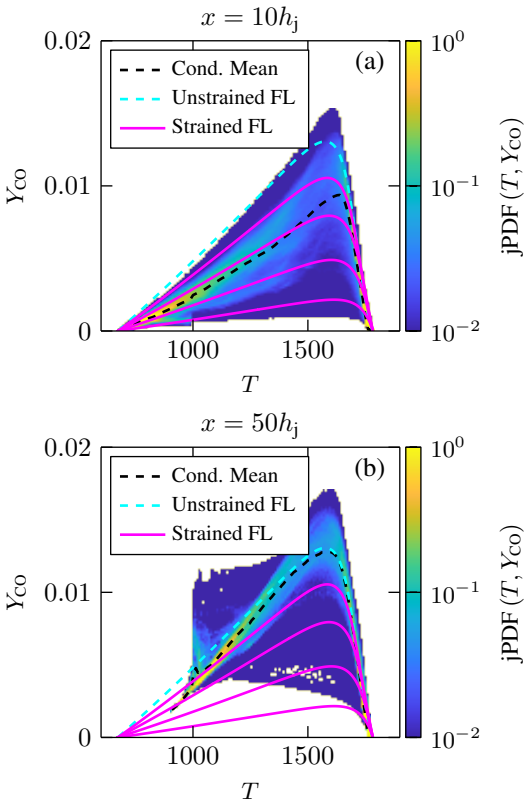

Fig. 5: Joint distribution of CO and T at $10h_j$ (a) and at $50h_j$ (b). The scatter plot shows the jPDF of the DNS data. Unstrained (- - -) and several increasingly strained (——) flamelets are shown as comparison.

unstrained flamelet reproduces the CO concentration well and the scatter of the DNS data is reduced. The area of high CO concentration at low temperature can be directly linked to the reduction in enthalpy. Fig. 6 shows the evolution of the enthalpy defect, defined as $\Delta h = h_{DNS} - h_{adiabatic}$ and the Karlovitz number over the streamwise location. Both quantities are surface-averaged on the progress variable surface corresponding to the maximum heat release in the unstretched flamelet ($C = 0.1236$). The Karlovitz number is the ratio between the timescales of the flame τ_F and the Kolmogorov timescale τ_η defined as $Ka = \tau_F/\tau_\eta$ [24] and used here as a measure of the local strain. Luca et al. [22] found that strain in turbulent premixed flames normalized by the Kolmogorov timescale is approximately constant ($a \cdot \tau_\eta \approx 0.23$) independent of the Reynolds number. Apart from a short increase at $x/h_j = 10$ due to the spreading of the jets, the Karlovitz number decreases along the flame length, thus confirming that the flame becomes less strained downstream. The behavior of the enthalpy is more complex. After an initial drop due to the recirculation of cold burnt products in the corners of the domain, the enthalpy begins increasing slightly as the

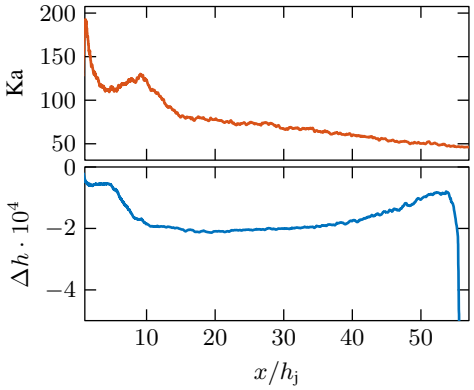

Fig. 6: Evolution of the Karlovitz number and the enthalpy defect over the streamwise location.

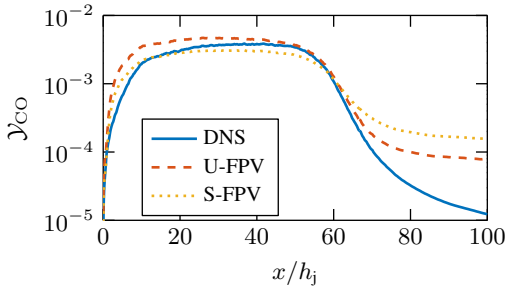

Fig. 7: Average CO flux in the domain compared to CO flux calculated from the unstrained (U-FPV) and the strained (S-FPV) models.

unburnt gas ($T^u < T_w$) flows along the wall and is heated. This heat flux is reversed abruptly at the flame tip when the hot flame interacts with the wall.

The surface-averaged strain on the flame surface is $a = 15\,000\,\mathrm{s}^{-1}$. We use the FlameMaster program [25] to calculate a 1D strained flamelet in a fresh-to-burnt counterflow configuration matching the conditions in the DNS [21]. The FPV model with the strained flamelet matches the DNS data better than the unstrained FPV model in the first half of the domain (Fig. 7) indicating the importance of the effects of strain rate on the formation of CO. Some deviations between the FPV model are expected, as an ensemble of flamelets is needed for an accurate prediction [17].

3.4. CO oxidation

In this section, the discrepancy of the FPV models and the DNS towards the end of the combustor are discussed. The timescale associated with CO oxidation is larger than the reaction rates of progress variable and the production of CO, so the introduced FPV models cannot adequately represent the oxidation of CO. Thus, the production and consumption of CO are analyzed in detail and the suitability of several parameters to describe CO oxidation is investigated. The optimal estimator analysis [26] has proven to be a useful tool in this process. It quantitatively assesses the capability of a set of parameters ψ, e.g. $\psi = [C, Y_{CO}]$, to parameterize $\dot{\omega}_{CO}$ by means of the irreducible error. The latter describes the fluctuations of $\dot{\omega}_{CO}$ with respect to the conditional mean $\langle \dot{\omega}_{CO} | \psi \rangle$, which represents the best possible representation given the chosen set of parameters. Hence, small irreducible errors indicate a good parameterization of $\dot{\omega}_{CO}$.

Concerning the accuracy of the numerical methods employed to compute the irreducible error: In a low-dimensional setting, with only one or two parameters used to compute the conditional mean (e.g. $\langle \dot{\omega}_{CO} | C \rangle$), the error is easily obtained using binning and histograms. However, it has been shown that an artificial neural network (ANN) produces more accurate results than a histogram technique once more than two input parameters are involved. A comparison between histogram and ANN is included in the supplementary material. A shallow ANN (one hidden layer) is used to compute conditional means in several dimensions. It should be pointed out that the ANN is not used in any modeling sense, but instead as a tool for data analysis. Further details on the optimal estimator are found in Berger et al. [26].

In addition to the progress variable C, the local CO mass fraction Y_{CO}, the enthalpy defect Δh, and the OH mass fraction Y_{OH} are considered. The CO mass fraction is included because the consumption of CO scales with the CO concentration: Assuming a general reaction $\mathrm{A} + \mathrm{B} \rightleftharpoons \mathrm{CO} + \mathrm{D}$, the change in CO concentration is given by the equation $\partial C_{CO}/\partial t = k_f C_A C_B - k_b C_{CO} C_D$. Splitting the source term into a production term $\dot{\omega}^+_{CO} = k_f C_A C_B$ and a consumption term $\dot{\omega}^-_{CO} = k_b C_{CO} C_D$, it becomes clear that the production of CO is independent of the local concentration, while the consumption is linearly dependent on the CO concentration. The enthalpy defect accounts for wall heat loss. Including the OH radical in the parameter space has two advantages. First, Knudsen et al. [23] have shown that OH is a unique and well-resolved parameterization of strain. Second, the OH radical is expected to be well correlated with the CO source term because OH is the reaction partner in the main CO oxidation reaction,

$$\mathrm{CO} + \mathrm{OH} \rightleftharpoons \mathrm{CO_2} + \mathrm{H}\,. \tag{3}$$

Table 2 lists all parameter sets and the domain-averaged irreducible errors for each location and each parameter set. The errors are normalized with the error in the full domain using only a progress variable and indicate the improvement achievable with the various parameters.

Fig. 8 shows the irreducible errors conditionally averaged w.r.t. the progress variable and normalized by the maximum CO source term from the unstretched flamelet. Four locations in the domain are investigated, two crosswise locations and two streamwise locations: (a) far from the wall in the center of the domain; (b) at the wall within one jet width of the wall; (c) $x/h_j = 10$ close to the inlet; (d) $x/h_j = 50$

Table 2: Domain-averaged irreducible errors for several parameter sets at different locations, normalized by the error for the full domain with only C.

	full domain	far from the wall	at the wall	inlet	flame tip
C	1	0.238	1.020	0.807	1.169
C, Y_{CO}	0.722	0.155	0.701	0.466	0.886
$C, \Delta h$	0.878	0.203	0.505	0.659	0.833
$C, Y_{\mathrm{CO}}, \Delta h$	0.563	0.149	0.345	0.427	0.678
C, Y_{OH}	0.455	0.103	0.398	0.295	0.518
$C, Y_{\mathrm{CO}}, \Delta h, Y_{\mathrm{OH}}$	0.256	0.084	0.155	0.221	0.314

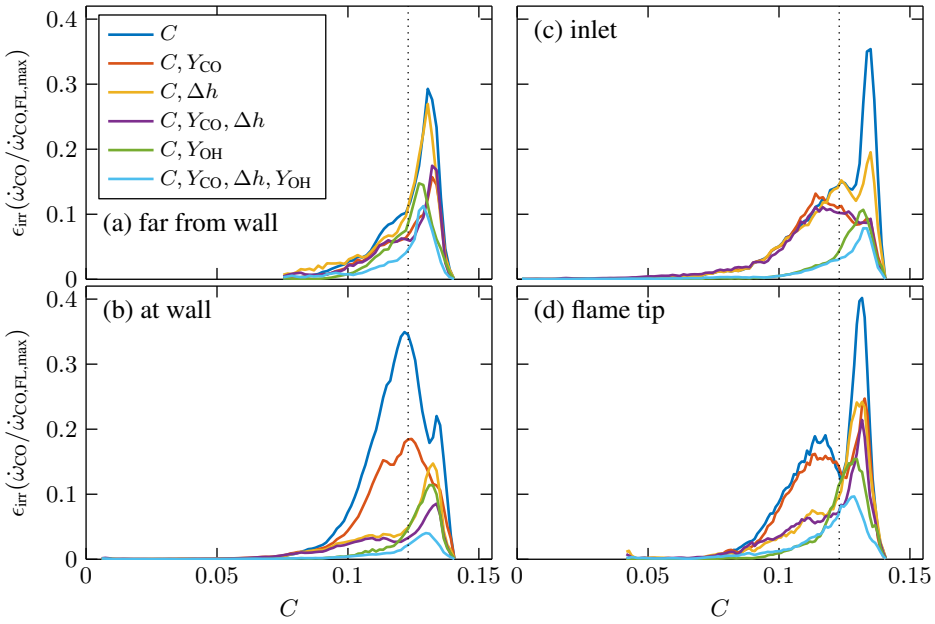

Fig. 8: Irreducible errors of the CO source term (a) far from the wall, (b) at the wall, (c) at $x = 10h_{\mathrm{j}}$, and (d) at $x = 50h_{\mathrm{j}}$, when using various parameter sets. The surface of peak heat release is indicated by the vertical dotted line.

close to the flame tip. The flame surface (defined by the peak heat release) is indicated by the vertical dotted line in the figure. In Fig 8(a), the error far from the wall is shown. In the domain center, where combustion is not greatly disturbed by the walls, the errors occur late in the combustion progress. Including Y_{CO} reduces the domain-averaged error by 1/3 and the peak local error by 1/2 compared to the prediction with only the progress variable. Enthalpy has very little effect far from the wall, confirming that the combustion is not affected by heat losses in this region. The addition of Y_{OH} further improves the correlation with $\dot{\omega}_{\mathrm{CO}}$, especially towards the very end of the combustion. Fig. 8(b) shows the irreducible error close to the wall. The errors are larger and occur earlier in the combustion progress. Including Y_{CO} has a similar effect as it does far from the wall: 30% reduction of the domain-averaged error and 50% reduction of the peak local error. Close to the wall, the heat loss influences the combustion more strongly. Adding enthalpy to the parameter set reduces both the average error and the peak local error by another 50% (2/3 reduction vs. single progress variable). The largest relative improvement is achieved by the full parameter set close to the wall, indicating that the physics in this region are particularly complex. In the upstream part of the domain (Fig. 8(c)), the source term is best parameterized by Y_{OH}, which confirms the findings that strain is especially important in this region. Y_{CO} has a stronger influence than Δh, while at the flame tip (Fig. 8(d)), this correlation is reversed and the effect of Y_{OH} is reduced. This demonstrates that the interactions between strain, enthalpy, and CO oxidation evolve throughout the domain.

The irreducible error calculated for the entire domain is shown in Fig. 9. Clearly, the error is a combination of the errors from the separate locations. The areas of strong influence of Y_{CO} and Δh are split between the center and the wall and by the combustion progress. The wall heat loss has a stronger influence in the unburnt, while the CO transport becomes more important in the burnt region. A similar split is observed between streamwise locations: Early in the domain $\dot{\omega}_{\mathrm{CO}}$ correlates better with Y_{CO}, but as the FWI

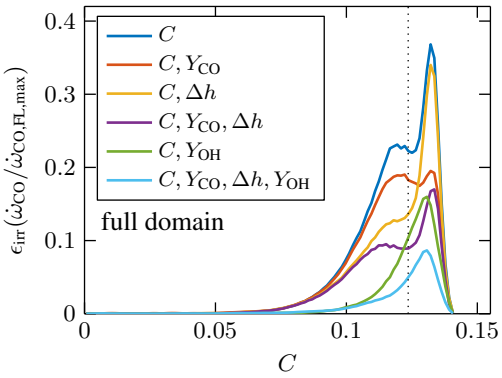

Fig. 9: Irreducible error of the CO source term in the whole domain when using various parameter sets. The surface of peak heat release is indicated by the vertical dotted line.

increases downstream, Δh becomes more important. Y_{OH} describes $\dot{\omega}_{\mathrm{CO}}$ well throughout the domain. The two regions where the influence is largest are the upstream part of the domain with high strain rates and close to the wall, where the availability of OH is reduced because of lower temperatures. In most domains and applications, Y_{CO} and Δh must both be taken into account when investigating CO emissions; very good results can be achieved with the addition of the OH radical.

4. Conclusion

We performed a DNS of premixed, turbulent methane-air jets in a domain enclosed by isothermal walls. The domain was designed to replicate conditions relevant to stationary gas turbine combustors. Strong interactions occur between the flame and the wall, recirculation regions develop, and the flame is strongly strained at the edges of the jets. All of these phenomena affect CO production and consumption. Strain effects are present mostly in the upstream part of the domain. FWI and wall heat losses have the strongest influence close to the wall and further downstream, while the long chemical timescales of CO compared to the FPV delay the oxidation of CO in the whole domain. We introduced and analyzed a dataset combining several difficulties faced in the modeling of CO emissions. The OH radical plays a particularly important role in a system with strained flames and CO emissions. On the one hand it is used to parameterize strain, on the other hand it the the main reaction partner for CO oxidation. However, despite the unquestionable advantages in parameterizing some of the important effects, the usefulness of solving a transport equation for this radical and using an even larger chemistry table need to be explored in a-posteriori tests. It was shown that the combination of these parameters was able to improve the irreducible error.

One possible modeling approach is a 2D tabulation, using the progress variable C and the enthalpy defect Δh. The table is combined with a transport equation for the CO mass fraction Y_{CO}, where the CO source term $\dot{\omega}_{\mathrm{CO}}$ is retrieved from the table and scaled with the local CO mass fraction. However, this approach ignores the influence of the OH radical on CO oxidation and the influence of strain. Thus, the model may need to be extended to a 3D chemistry table with flamelets at various strain rates. The third dimension is parameterized by the OH mass fraction Y_{OH}, which in turn necessitates a transport equation for OH, analogous to the CO transport equation. The OH source term $\dot{\omega}_{\mathrm{OH}}$ is retrieved from the table and may also benefit from scaling. The total additional cost of this approach is a 3D chemistry table and two transport equations. Another option that we will investigate in future work is the parameterization of enthalpy by the OH radical with a subsequent energy correction, since the concentration of OH is sensitive to high cooling rates [27]. This may help reduce the dimensionality of the tabulation. Another method to avoid high-dimensional tables may be a hybrid modeling approach with individual, lower-dimensional tables, conditioned on different flow regions. The obvious advantage of this approach is the reduction in tabulation effort and more rapid access to the tabulated values. On the other hand, this approach requires more detailed a-priori knowledge of the flow field. Furthermore, discontinuities at the boundaries between flow regions must be considered, and the blending procedure between two tables requires a detailed analysis. Which specific model provides the most accurate prediction may additionally be case dependent. A general difficulty of CO modeling comes from the very low emission limits prescribed by legal regulations, since the equilibrium concentrations are in the same order of magnitude as the emissions limits. Presumably, complex models and/or high-dimensional tables are necessary for the desired accuracy. Future work will focus on formalizing models to account for the physical phenomena discussed here.

Acknowledgments

Generous support of the Deutsche Forschungsgemeinschaft (DFG) under grant number PI 368/25-1 and the Research Association for Combustion Engines (FVV) under grant number 6013970 is gratefully acknowledged. The authors gratefully acknowledge the Gauss Centre for Supercomputing e.V. (www.gauss-centre.eu) for funding this project by providing computing time on the GCS Supercomputer SuperMUC-NG at Leibniz Supercomputing Centre (www.lrz.de).

References

[1] A. Andreini, B. Facchini, Gas turbines design and off-design performance analysis with emissions evaluation, J. Eng. Gas Turbines Power 126 (1) (2004) 83–91. doi:10.1115/1.1619427.

[2] M. Lipperheide, M. Gassner, F. Weidner, S. Bernero, M. Wirsum, Long-term carbon monoxide emission behavior of heavy-duty gas turbines: An approach for

model-based monitoring and diagnostics, Int. J. Spray Combust. Dyn. 11 (2019) 1–14. doi:10.1177/1756827718791921.

[3] A. Dreizler, B. Böhm, Advanced laser diagnostics for an improved understanding of premixed flame-wall interactions, Proc. Combust. Inst. 35 (1) (2015) 37–64. doi:10.1016/j.proci.2014.08.014.

[4] M. Mann, C. Jainski, M. Euler, B. Böhm, A. Dreizler, Transient flame–wall interactions: Experimental analysis using spectroscopic temperature and CO concentration measurements, Combust. Flame 161 (9) (2014) 2371–2386. doi:10.1016/j.combustflame.2014.02.008.

[5] C. Jainski, M. Rißmann, B. Böhm, J. Janicka, A. Dreizler, Sidewall quenching of atmospheric laminar premixed flames studied by laser-based diagnostics, Combust. Flame 183 (2017) 271–282. doi:10.1016/j.combustflame.2017.05.020.

[6] S. Ganter, A. Heinrich, T. Meier, G. Kuenne, C. Jainski, M. C. Rißmann, A. Dreizler, J. Janicka, Numerical analysis of laminar methane–air side-wall-quenching, Combust. Flame 186 (2017) 299–310. doi:10.1016/j.combustflame.2017.08.017.

[7] A. Heinrich, S. Ganter, G. Kuenne, C. Jainski, A. Dreizler, J. Janicka, 3D numerical simulation of a laminar experimental SWQ burner with tabulated chemistry, Flow Turbul. Combust. 100 (2018) 535–559. doi:10.1007/s10494-017-9851-9.

[8] B. Jiang, R. L. Gordon, M. Talei, Head-on quenching of laminar premixed methane flames diluted with hot combustion products, Proc. Combust. Inst. 37 (4) (2019) 5095–5103. doi:10.1016/j.proci.2018.07.120.

[9] R. Palulli, M. Talei, R. L. Gordon, Unsteady flame–wall interaction: Impact on CO emission and wall heat flux, Combust. Flame 207 (2019) 406–416. doi:10.1016/j.combustflame.2019.06.012.

[10] B. Jiang, D. Brouzet, M. Talei, R. L. Gordon, Q. Cazeres, B. Cuenot, Turbulent flame-wall interactions for flames diluted by hot combustion products, Combust. Flame 230 (2021) 111432. doi:10.1016/j.combustflame.2021.111432.

[11] R. Palulli, D. Brouzet, M. Talei, R. Gordon, A comparative study of flame-wall interaction and flame-cooling air interaction, Int. J. Heat Fluid Flow 92 (2021) 108888. doi:10.1016/j.ijheatfluidflow.2021.108888.

[12] H. Kosaka, F. Zentgraf, A. Scholtissek, L. Bischoff, T. Häber, R. Suntz, B. Albert, C. Hasse, A. Dreizler, Wall heat fluxes and CO formation/oxidation during laminar and turbulent side-wall quenching of methane and DME flames, Int. J. Heat Fluid Flow 70 (2018) 181–192. doi:10.1016/j.ijheatfluidflow.2018.01.009.

[13] D. V. Efimov, P. de Goey, J. A. van Oijen, QFM: Quenching flamelet-generated manifold for modelling of flame–wall interactions, Combust. Theory Model. 24 (1) (2020) 72–104. doi:10.1080/13647830.2019.1658901.

[14] S. Popp, S. Hartl, D. Butz, D. Geyer, A. Dreizler, L. Vervisch, C. Hasse, Assessing multi-regime combustion in a novel burner configuration with large eddy simulations using tabulated chemistry, Proc. Combust. Inst. 38 (2) (2021) 2551–2558. doi:10.1016/j.proci.2020.06.098.

[15] M. Ihme, H. Pitsch, Modeling of radiation and nitric oxide formation in turbulent nonpremixed flames using a flamelet/progress variable formulation, Phys. Fluids 20 (5) (2008). doi:10.1063/1.2911047.

[16] P. Trisjono, K. Kleinheinz, S. Kang, H. Pitsch, Large eddy simulation of stratified and sheared flames of a premixed turbulent stratified flame burner using a flamelet model with heat loss, Flow Turbul. Combust. 92 (2014) 201 – 235. doi:10.1007/s10494-013-9522-4.

[17] W. Han, H. Wang, G. Kuenne, E. R. Hawkes, J. H. Chen, J. Janicka, C. Hasse, Large eddy simulation/dynamic thickened flame modeling of a high Karlovitz number turbulent premixed jet flame, Proc. Combust. Inst. 37 (2) (2019) 2555–2563. doi:10.1016/j.proci.2018.06.228.

[18] S. B. Pope, Turbulent Flows, Cambridge University Press, Cambridge, 2000. doi:10.1017/CBO9780511840531.

[19] O. Desjardins, G. Blanquart, G. Balarac, H. Pitsch, High order conservative finite difference scheme for variable density low Mach number turbulent flows, J. Comput. Phys. 227 (15) (2008) 7125 – 7159. doi:10.1016/j.jcp.2008.03.027.

[20] L. Cai, A. Ramalingam, H. Minwegen, K. A. Heufer, H. Pitsch, Impact of exhaust gas recirculation on ignition delay times of gasoline fuel: An experimental and modeling study, Proc. Combust. Inst. 37 (1) (2019) 639–647. doi:10.1016/j.proci.2018.05.032.

[21] E. R. Hawkes, J. H. Chen, Comparison of direct numerical simulation of lean premixed methane–air flames with strained laminar flame calculations, Combust. Flame 144 (1) (2006) 112–125. doi:10.1016/j.combustflame.2005.07.002.

[22] S. Luca, A. Attili, E. Lo Schiavo, F. Creta, F. Bisetti, On the statistics of flame stretch in turbulent premixed jet flames in the thin reaction zone regime at varying Reynolds number, Proc. Combust. Inst. 37 (2) (2019) 2451–2459. doi:10.1016/j.proci.2018.06.194.

[23] E. Knudsen, H. Kolla, E. R. Hawkes, H. Pitsch, LES of a premixed jet flame DNS using a strained flamelet model, Combust. Flame 160 (12) (2013) 2911–2927. doi:10.1016/j.combustflame.2013.06.033.

[24] N. Peters, Turbulent Combustion, Cambridge University Press, Cambridge, 2000.

[25] H. Pitsch, A C++ computer program for 0D combustion and 1D laminar flame calculations - FlameMaster.

[26] L. Berger, K. Kleinheinz, A. Attili, F. Bisetti, H. Pitsch, M. E. Mueller, Numerically accurate computational techniques for optimal estimator analyses of multi-parameter models, Combust. Theory Model. 22 (3) (2018) 480–504. doi:10.1080/13647830.2018.1424353.

[27] J. R. Creighton, Dependence of CO emissions on the rate of product cooling, Combust. Flame 123 (3) (2000) 402–411. doi:10.1016/S0010-2180(00)00160-7.